Supplementary Information (SI) for Journal of Materials Chemistry A.

Decorating unsaturated iron-nitrogen coordination sites with small-sized iron selenide nanoparticles for highly efficient oxygen reduction catalysis

Weicheng Zhang, Xinzhu Li, Shunhua Guo, Zixiang Wan, Le Huang, Zhicong Shi, Naiguang Wang*

School of Materials and Energy, Guangdong University of Technology, Guangzhou, 510006, China.

Experimental Section

Chemicals

All reagents used in the experiments were of analytical grade and obtained from reliable suppliers. Specifically, zinc nitrate hexahydrate, 2-methylimidazole, isopropanol, melamine, potassium hydroxide, ethanol, and iron (III) acetylacetonate were purchased from Aladdin, while commercial Pt/C (20 wt%) and Nafion solution (5 wt%) were supplied by Sigma-Aldrich. Deionized water, purified using a Milli-Q system, was also utilized throughout all experimental procedures to ensure consistency and reliability.

Physical Characterization

The phases of all synthesized catalysts were identified using an X-ray diffractometer (XRD, D8 ADVANCE) equipped with Cu-K_α radiation source. The 2θ range was set from 10° to 80°, with a scanning rate of 10° $\min^{-1}$. The degree of disorder in the carbon support for each catalyst was assessed adopting a micro-confocal Raman spectrometer (LabRAM HR Evolution) fitted with He and Cd ion lasers. The Raman shift varied from 1000 to 2400 cm^{-1} and the exciting radiation wavelength was 532 nm. The specific surface areas and pore diameters of these catalysts were determined via nitrogen isothermal adsorption/desorption measurements, conducted at 77.3 K with a specific surface and pore size analyzer (3H-2000PS1). The chemical constitutions on the specimen surfaces were detected with an X-ray photoelectron spectroscopy (XPS, Escalab 250Xi), while the contents of Fe and Se were measured through an inductively coupled plasma atomic emission spectrometry (ICP-AES, Aglient−5110). Scanning electron microscope (SEM, Apreo 2S HiVac) and transmission electron microscopy (TEM, Thermo Fisher Scientific-Tecnai G2 F20) were employed to investigate the morphologies and microstructural characteristics of the catalysts.

Fe K-edge X-ray absorption fine structure (XAFS) analyses were conducted at the BL14W beamline of the Shanghai Synchrotron Radiation Facility (SSRF) in China, utilizing Si(111) crystal monochromators. Prior to beamline analysis, samples were mounted in aluminum holders and sealed with Kapton tape. Room-temperature XAFS spectra were acquired using a 4-channel Silicon Drift Detector (SDD), model Bruker 5040. The Fe K-edge extended X-ray absorption fine structure (EXAFS) spectra were collected in transmission mode. Notably, minimal variations in the line shape and peak position of the Fe K-edge XANES spectra were observed across two consecutive scans of a specific sample. The XAFS spectra of standard samples were also recorded in transmission mode.

Electrochemical measurements

The ORR catalytic performance of the synthesized catalysts was evaluated through electrochemical measurements, utilizing a CHI750E electrochemistry workstation and a three-electrode system. A carbon rod and an Ag/AgCl electrode were served as the counter and reference electrodes, respectively. The working electrode was a rotating ring-disk electrode (RRDE) featuring a circular glassy carbon substrate ($\Phi = 4$ mm) coated with a catalyst film. This film was prepared from the ink containing 4 mg of catalyst, 590 μL of isopropanol, 390 μL of deionized water, and 20 μL of 5 wt% Nafion solution, after undergoing ultrasonic treatment. For comparison, commercial Pt/C (20 wt%) was used as a benchmark, with each catalyst loaded at a density of 0.4 mg cm^{-2} on the glassy carbon. The electrolytes adopted here were 0.1 M KOH and 3.5 wt% NaCl, each saturated with O_2, and prepared from analytically pure reagents and deionized water. All potentials in this work were calibrated to the reversible hydrogen electrode (RHE) using the following equation:

$$E_{\mathrm{RHE}} = E_{\mathrm{Ag/AgCl}} + 0.197 + 0.059\ \mathrm{pH} \tag{1}$$

Prior to the electrochemical measurements, cyclic voltammetry (CV) was conducted at a scan rate of 100 mV s^{-1} for a minimum of 40 cycles. This process aimed to stabilize the catalyst surfaces and achieve a steady state. Subsequently, the CV curves were recorded in both O_2 and Ar saturated electrolytes at a scan rate of 50 mV s^{-1}. Additionally, the double-layer capacitances (C_{dl}) were determined from these CV curves in non-Faradaic potential regions by varying the scan rates from 10 to 50 mV s^{-1}. For measuring the ORR polarization curves, linear sweep voltammetry (LSV) was employed with the electrode rotating at 1600 rpm and a scan rate of 10 mV s^{-1}. The LSV experiments covered the potential ranges of 0.20−1.10 V (*vs*. RHE) in 0.1 M KOH and 0.10−0.90 V (*vs*. RHE) in 3.5 wt% NaCl. Afterward, the kinetic current densities (J_{K}) were calculated from these ORR polarization curves using the Koutecky-Levich equation:

$$\frac{1}{J_{\mathrm{D}}} = \frac{1}{J_{\mathrm{K}}} + \frac{1}{J_{\mathrm{L}}} \tag{2}$$

where J_{D} and J_{L} were the disk and limiting-diffusion current densities on the glassy carbon, respectively. The electron transfer number (n) and hydrogen peroxide yield (H_2O_2) were also determined based on the following equations:

$$n = 4 \times \frac{I_{\mathrm{D}}}{I_{\mathrm{D}} + \frac{I_{\mathrm{D}}}{N}} \tag{3}$$

$$H_2O_2\% = 200 \times \frac{\frac{I_{\mathrm{R}}}{N}}{I_{\mathrm{D}} + \frac{I_{\mathrm{R}}}{N}} \tag{4}$$

where I_{D} and I_{R} were disk and ring current, respectively, while N with the value of 0.4 was current collection efficiency on the gold ring of RRDE. The durability of catalysts can be assessed through accelerated degradation tests and chronoamperometric response. The accelerated degradation was examined by comparing the polarization curves before and after 5000 CV cycles; meanwhile, the chronoamperometric response was measured at 0.70 V (*vs*. RHE) over a period of 50000 s.

Performance testing of Mg-air and Zn-air batteries

The catalyst ink used for electrochemical measurements was also employed to prepare the air-electrodes for testing the performance of Mg-air and Zn-air batteries. Typically, each ink was uniformly coated onto a carbon cloth (W1S1010) for several times through a pipette gun. The wet carbon cloth was then dried at 60°C in a drying box and served as the air-electrode, with a catalyst loading of 1.0 mg cm^{-2}. The tested area, which had a diameter of 1.0 cm, was circular. A pure magnesium sheet and the prepared air-electrode were used as the anode and cathode, respectively, for a Mg-air battery. The battery was assembled using a home-made cell design, featuring a 5.0 cm distance between the two electrodes and utilizing 3.5 wt% NaCl aqueous solution as the electrolyte. Moreover, the fabrication of Zn-air battery was analogous to that of Mg-air battery, except that a pure zinc sheet was utilized as the anode while 6 M KOH containing 0.2 M $Zn(CH_3COO)_2$ served as the electrolyte. The battery performance was evaluated through the galvanostatic discharge at various current densities on a LANHE CT2001A battery testing system.

DFT theoretical calculations

All the theoretical calculations were performed via the Vienna ab initio simulation package (VASP) within the framework of density functional theory (DFT)[1], employing the Perdew-Burke-Ernzerhof (PBE) exchange-correlation functional of the generalized gradient approximation (GGA) and projector augmented wave (PAW) pseudopotentials [2–4]. To examine the effect of van der Waals interaction on reaction energetics, calculations were carried out using the DFT-D3 functional. VASP was implemented with high precision, and the cut-off energy for the plane-wave basis set was fixed at 500 eV. The Brillouin zone was sampled using the Monkhorst-Pack scheme with a k-point mesh of 1 × 1 × 1. When modeling the FeSe/Fe-NSC and Fe-NSC catalysts, 7 × 7 graphene supercells containing a Fe-N_2 moiety, with S-doping at the third coordination shell of Fe, were selected as the substrate for anchoring metal atoms. The (101) surface, featuring the most energetically favorable termination, is adopted as the active surface for FeSe. This model was constructed adopting a slab consisting of six atomic layers. The vacuum layer was set to 15 Å to ensure negligible interactions between the periodically repeated slabs. The fixed base vector optimization method of VASP ensures that the orientation of the vacuum layer in 2D materials was not optimized. Second-order Methfessel-Paxton smearing with a width of 0.1 eV was applied to set the partial occupancies. The geometry optimizations were completed when the convergence criteria for the total energy of electron self-consistent field and the forces reached 10^{-6} eV and -0.03 eV $Å^{-1}$, respectively. The potential dependence of reaction free energies for elementary steps involving proton-electron transfers was evaluated using the computational hydrogen electrode (CHE) method. In this approach, a reversible hydrogen electrode (RHE) served as the reference electrode.

The Gibbs free energy was calculated according to the following equation:

$$\Delta G = E_{\mathrm{DFT}} + \Delta \mathrm{ZPE} - T\Delta S + \Delta G_{\mathrm{U}} \tag{5}$$

where G referred to the Gibbs free energy, E_{DFT} was the electronic energy obtained from DFT calculations, ZPE represented the zero-point energy, and T denoted the temperature set at 298.15 K. The change in Gibbs free energy, ΔG_{U}, can be calculated as

$$\Delta G_{\mathrm{U}} = - eU \tag{6}$$

where U corresponded to the potential of the photogenerated electrons/holes with respect to the normal hydrogen electrode (NHE), and e represented the number of transferred electrons.

To determine the ORR catalytic performance, the adsorption energies of the relevant adsorbates were calculated based on the following equation:

$$E_{\mathrm{ads}} = E_{\mathrm{total}} + E_{\mathrm{slab}} - E_{\mathrm{adsorbate}} \tag{7}$$

where E_{ads} was the adsorption energy, E_{total} represented the total energy of this system with adsorbate, E_{slab} denoted the energy of optimized slab, and $E_{\mathrm{adsorbate}}$ was the energy of isolated adsorbate in gas phase.

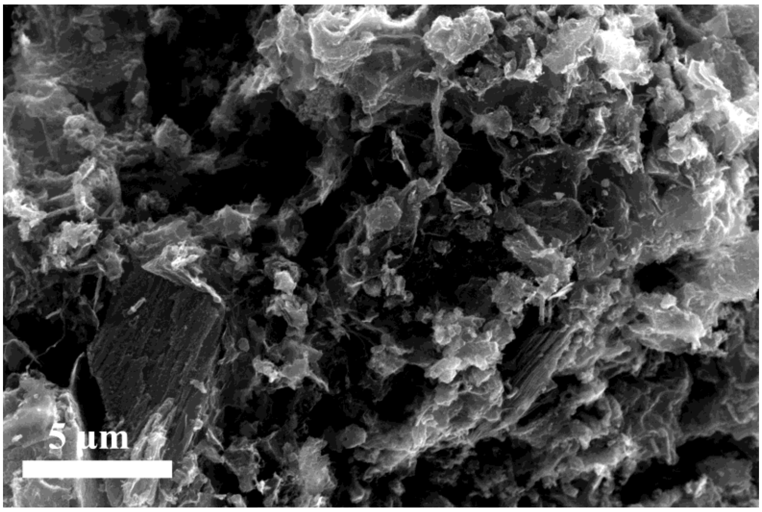

Fig. S1 SEM image of Fe-NSC.

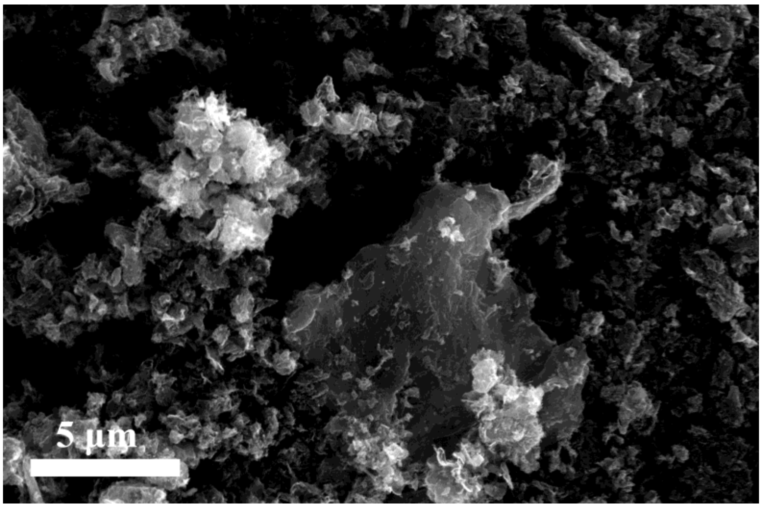

Fig. S2 SEM image of NSC.

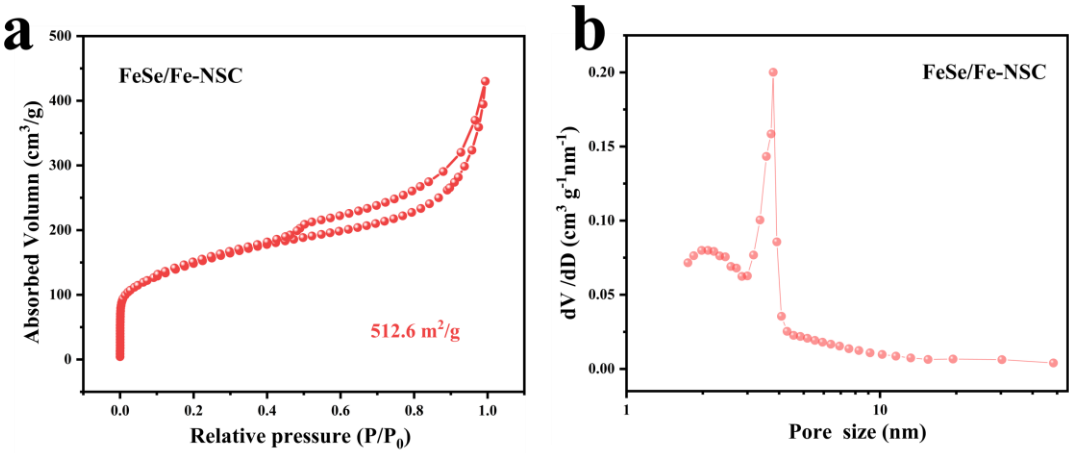

Fig. S3 (a) N_2 adsorption-desorption isotherms and (b) pore-size distributions of FeSe/Fe-NSC.

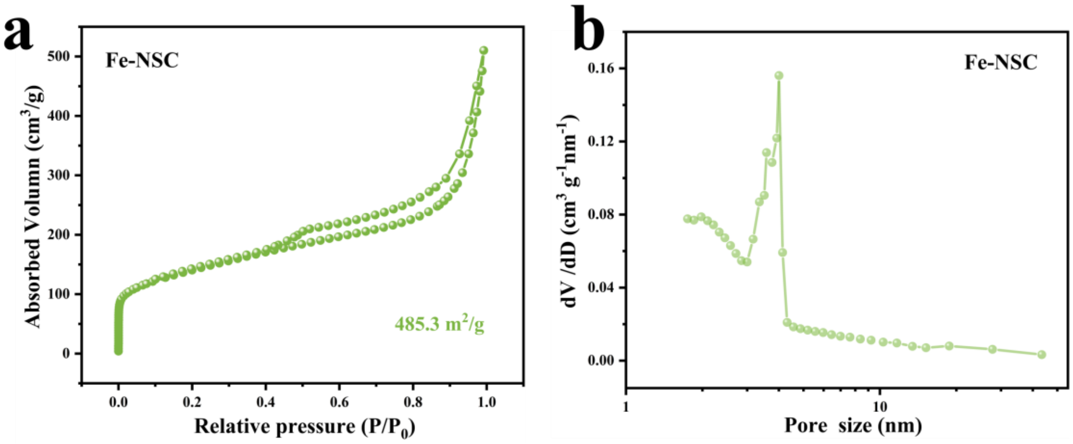

Fig. S4 (a) N_2 adsorption-desorption isotherms and (b) pore-size distributions of Fe-NSC.

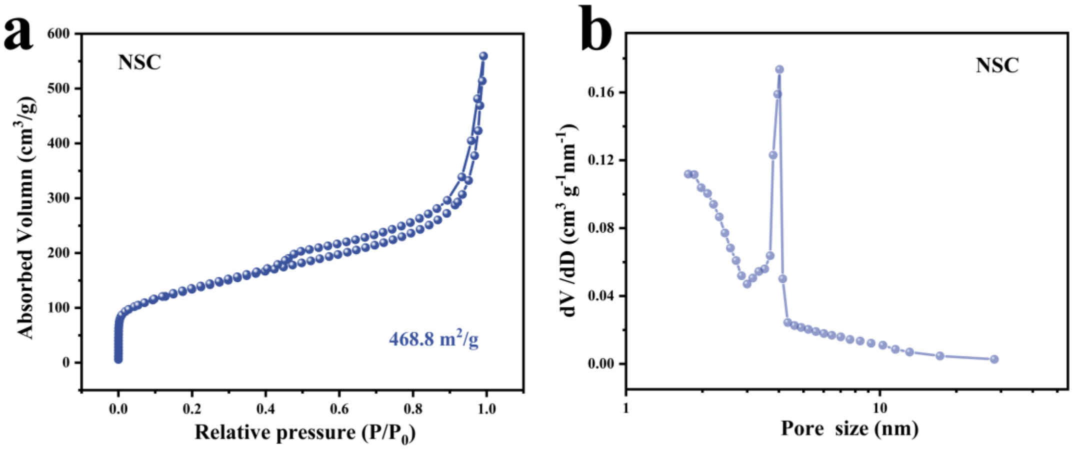

Fig. S5 (a) N_2 adsorption-desorption isotherms and (b) pore-size distributions of NSC.

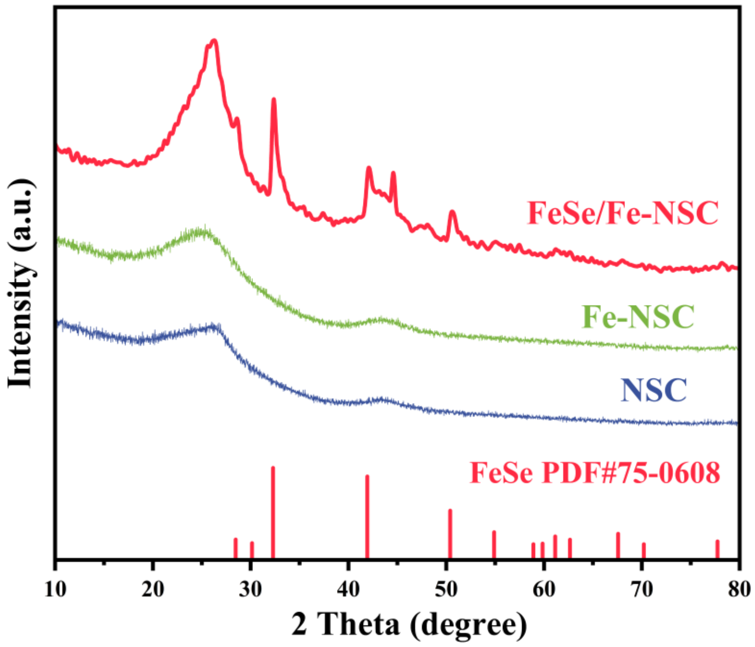

Fig. S6 XRD patterns of FeSe/Fe-NSC, Fe-NSC, and NSC.

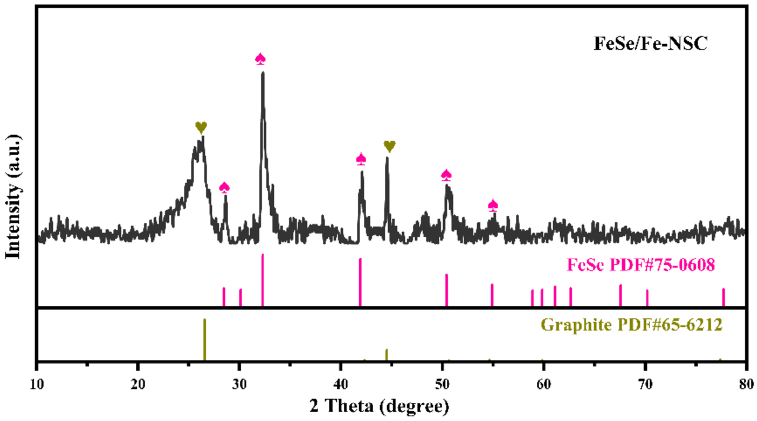

Fig. S7 Background-subtracted XRD pattern of FeSe/Fe-NSC.

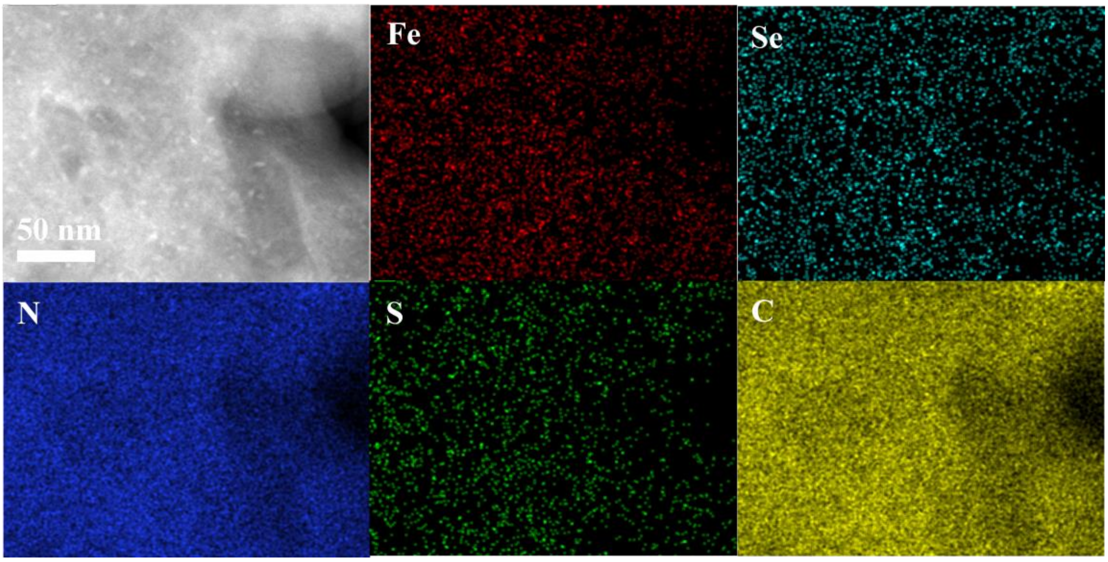

Fig. S8 EDS elemental mappings of FeSe/Fe-NSC.

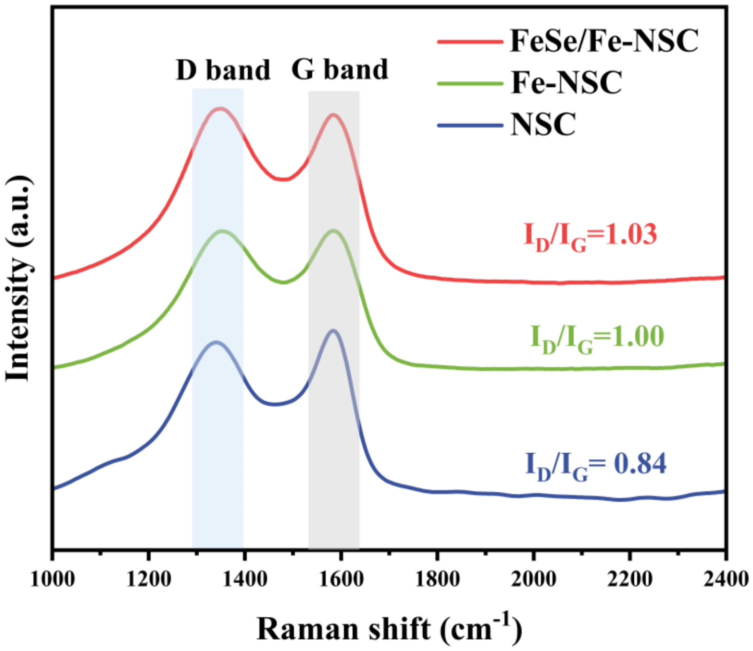

Fig. S9 Raman spectra of FeSe/Fe-NSC, Fe-NSC, and NSC.

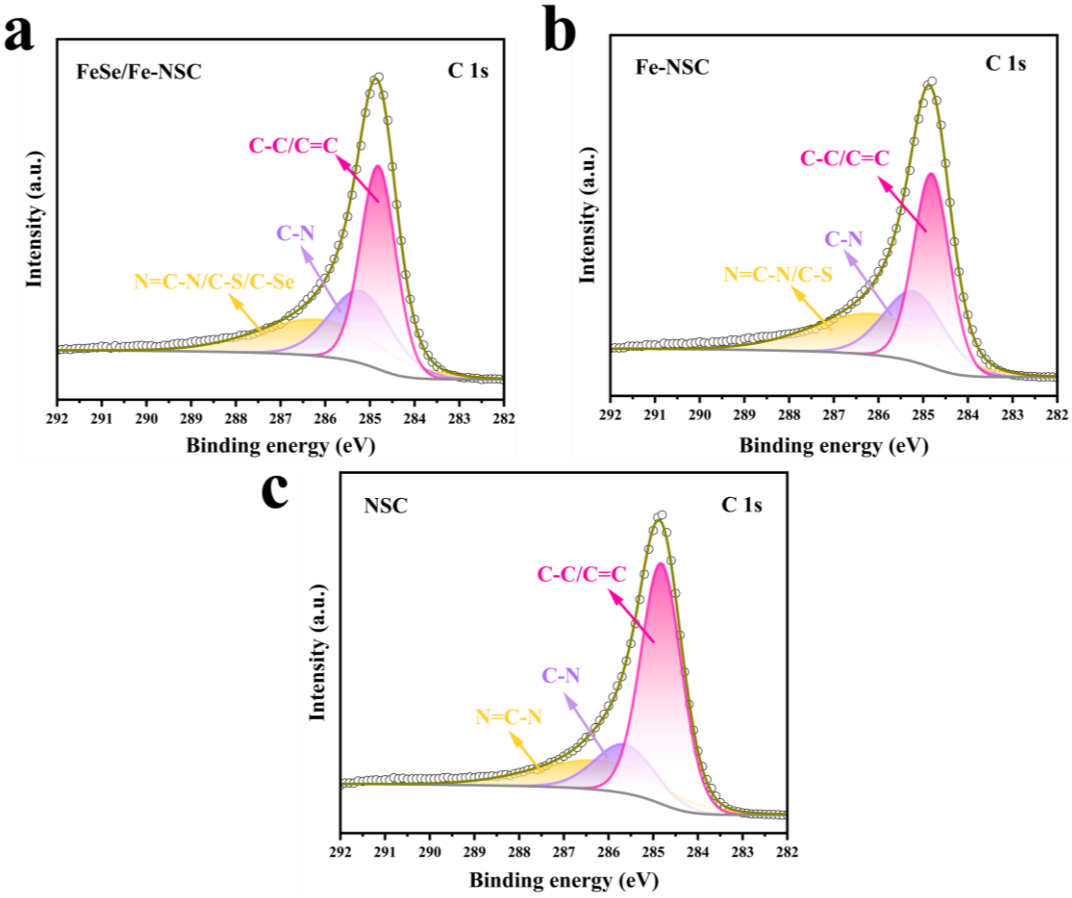

Fig. S10 High-resolution XPS of C 1s spectra for (a) FeSe/Fe-NSC, (b) Fe-NSC, and (c) NSC.

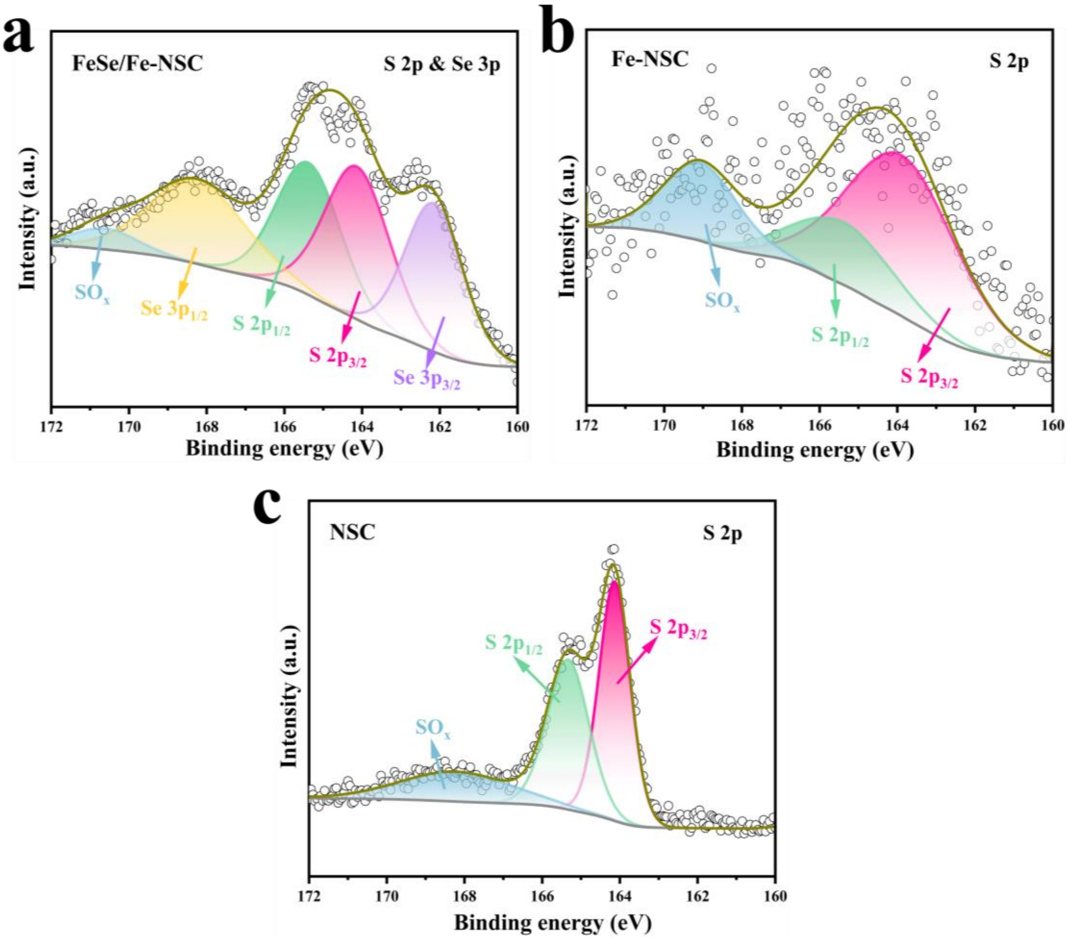

Fig. S11 High-resolution XPS of (a) S 2p and Se 3p spectra for FeSe/Fe-NSC, S 2p spectra for (b) Fe-NSC and (c) NSC.

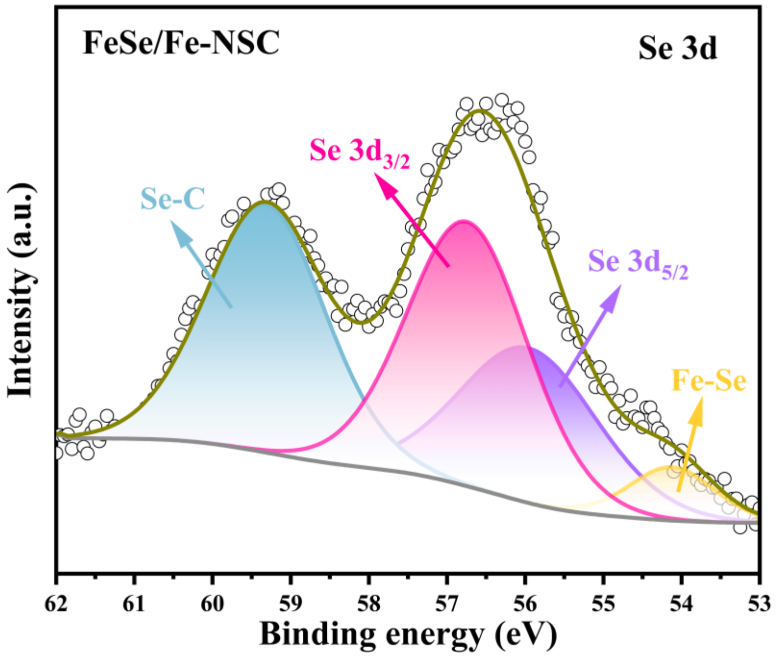

Fig. S12 High-resolution XPS of Se 3d spectra for FeSe/Fe-NSC.

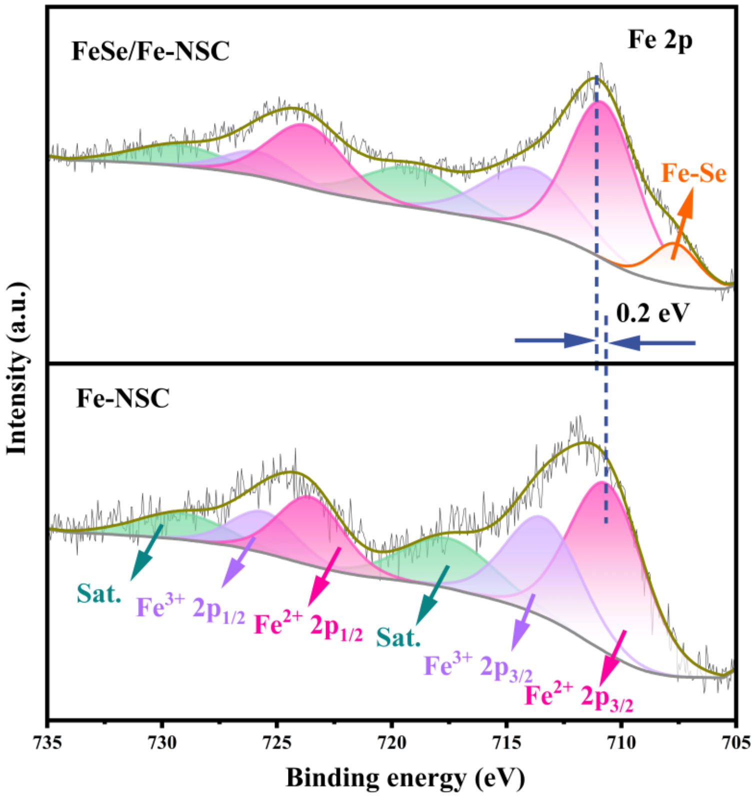

Fig. S13 High-resolution XPS of Fe 2p spectra for FeSe/Fe-NSC and Fe-NSC.

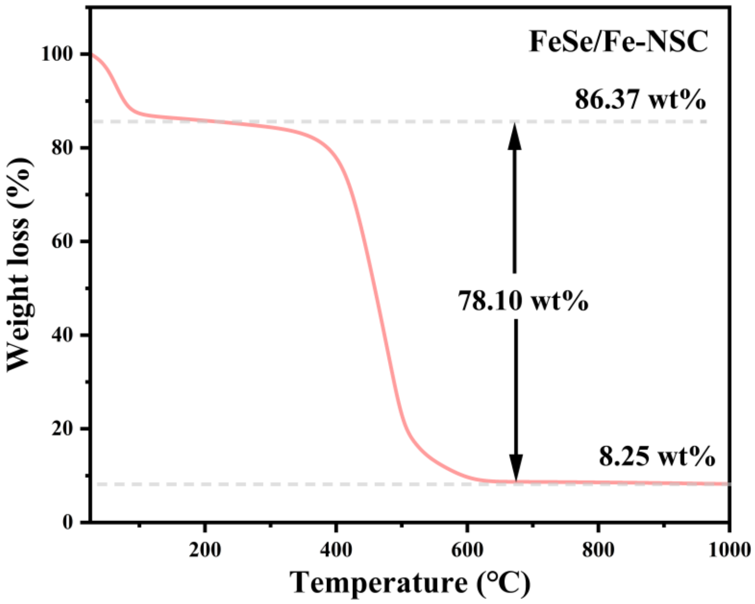

Fig. S14 TGA curve of FeSe/Fe-NSC under air atmosphere at a heating rate of 10°C min^{-1}.

The TGA results (Fig. S14) reveal an initial weight of 100 wt%, with a 13.63% weight loss from room temperature to 130°C, attributed to the evaporation of absorbed moisture. Subsequently, between 130°C and 1000°C, the sample undergoes a further 78.1% weight loss, leaving a residual mass of 8.25%. The observed weight loss corresponds to the conversion of iron species into Fe_2O_3 and the combustion of the carbon matrix.

Based on the conversion from Fe to Fe_2O_3, we calculate the iron content in FeSe/Fe-NSC to systematically quantify its compositional profile.

$$\text{FeSe/Fe-NSC} \rightarrow \text{Fe2O3} + \text{gas}$$

Atomic weight: Fe (56), Se (79), O (16)

$$\text{Fe wt\%} = 8.25 \times \frac{56\times2}{56\times2+16\times3} = 5.78 \text{ wt\%}$$

The analytical results indicate a final Fe content of 5.78 wt% in the composite. To validate the TGA findings, inductively coupled plasma atomic emission spectroscopy (ICP-AES) is employed to quantify Fe and Se contents (Table S4). The ICP-AES measurements confirm a Fe content of 5.75

wt%, showing excellent consistency with the TGA-derived value (deviation $< 0.5\%$), alongside a Se content of 4.06 wt%. Calculations based on these values reveal a Fe-to-Se atomic ratio approaching 2:1. Moreover, given the 1:1 atomic ratio of Fe to Se in FeSe, calculations reveal that the FeSe/Fe-NSC composite contains 6.93 wt% FeSe nanoparticles and 2.91 wt% isolated Fe single atoms. This quantitative analysis provides strong evidence for the coexistence of FeSe NPs and atomic Fe sites anchored on the N,S-codoped carbon matrix. The calculation procedure for determining the mass fraction of FeSe nanoparticles in the FeSe/Fe-NSC composite is as follows:

FeSe content = Se wt% × Molar mass of FeSe/Molar mass of Se = $4.06 \times (55.85 + 78.96)/78.96 = 6.93$ wt%.

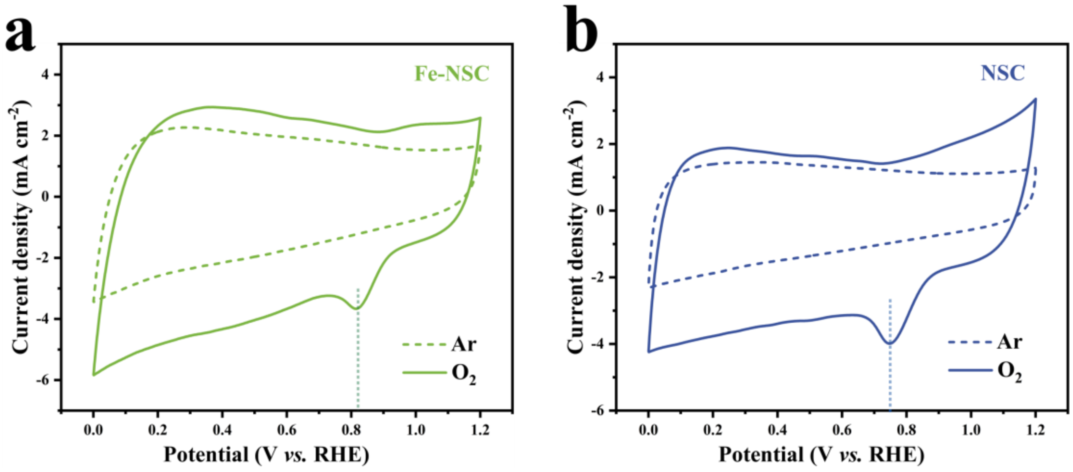

Fig. S15 CV curves of (a) Fe-NSC and (b) NSC in 0.1 M KOH.

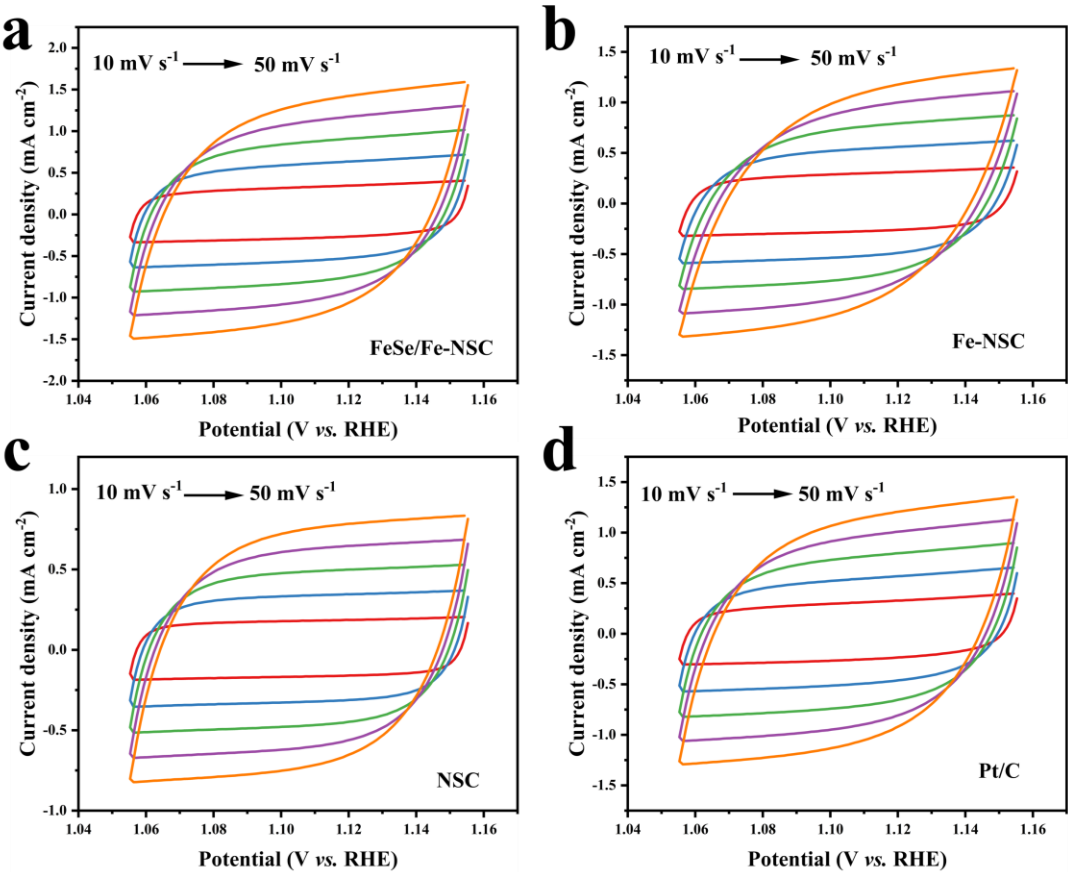

Fig. S16 CV curves of (a) FeSe/Fe-NSC, (b) Fe-NSC, (c) NSC, and (d) Pt/C in 0.1 M KOH.

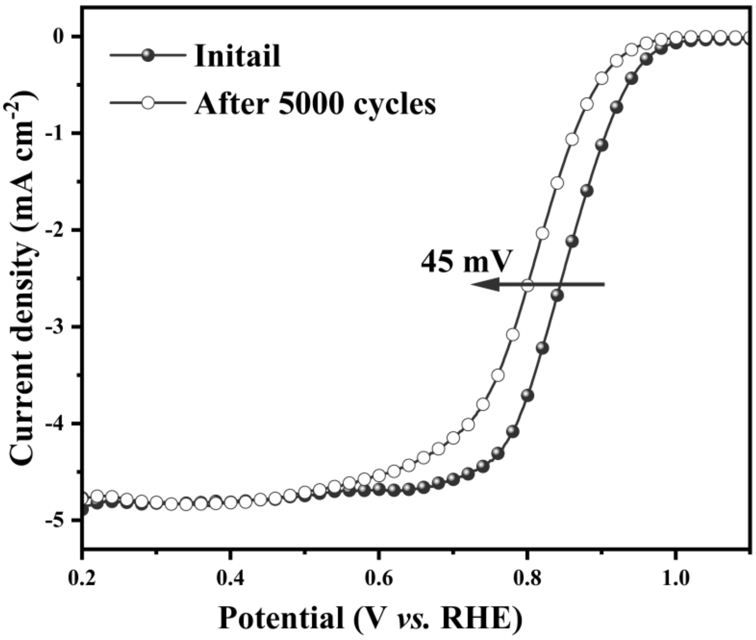

Fig. S17 LSV polarization curves of commercial Pt/C before and after 5000 CV cycles in 0.1 M KOH.

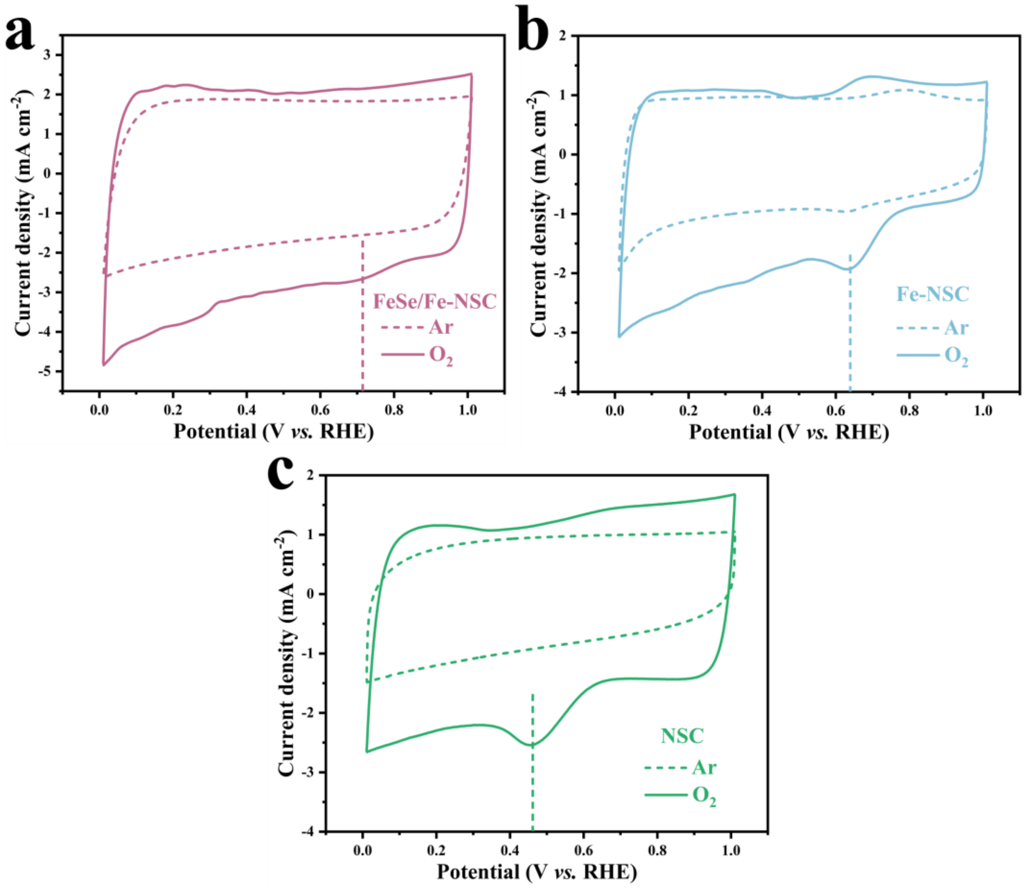

Fig. S18 CV curves of (a) FeSe/Fe-NSC, (b) Fe-NSC and (c) NSC in 3.5 wt% NaCl.

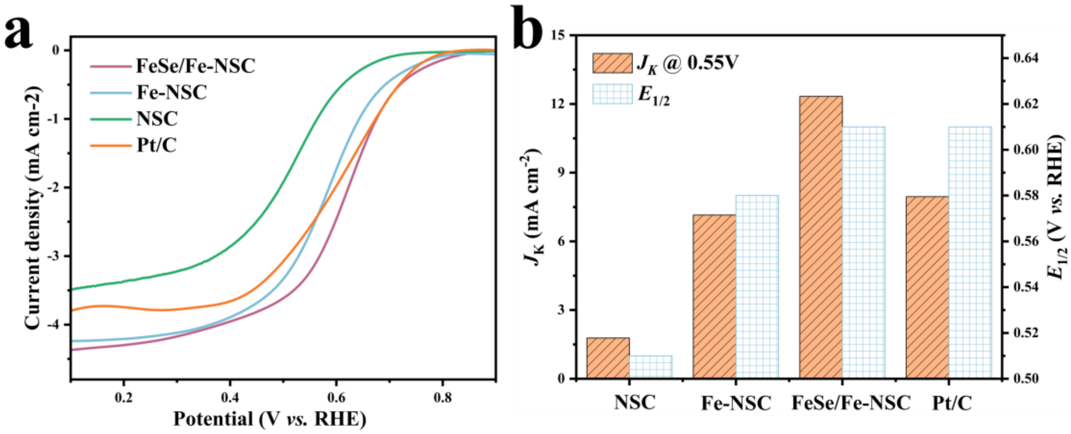

Fig. S19 (a) LSV polarization curves in 3.5 wt% NaCl and (b) corresponding $E_{1/2}$ and J_k values.

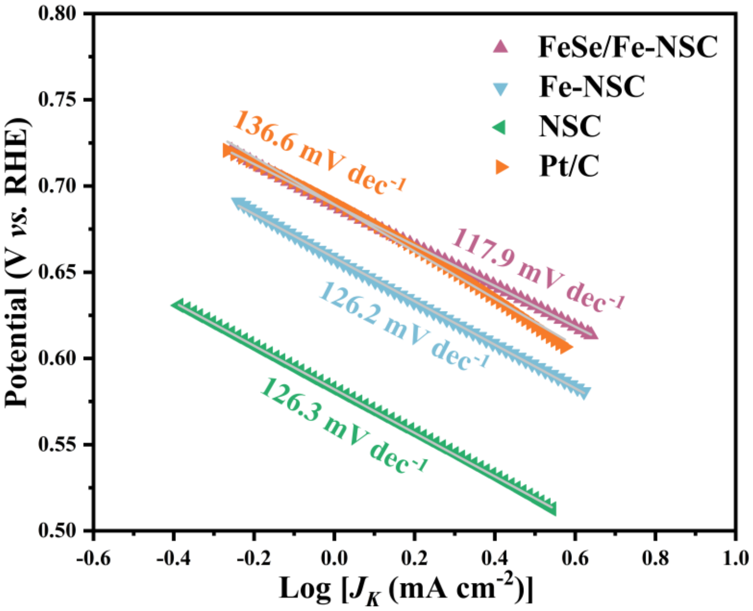

Fig. S20 Tafel plots of FeSe/Fe-NSC, Fe-NSC, NSC, and Pt/C in 3.5 wt% NaCl.

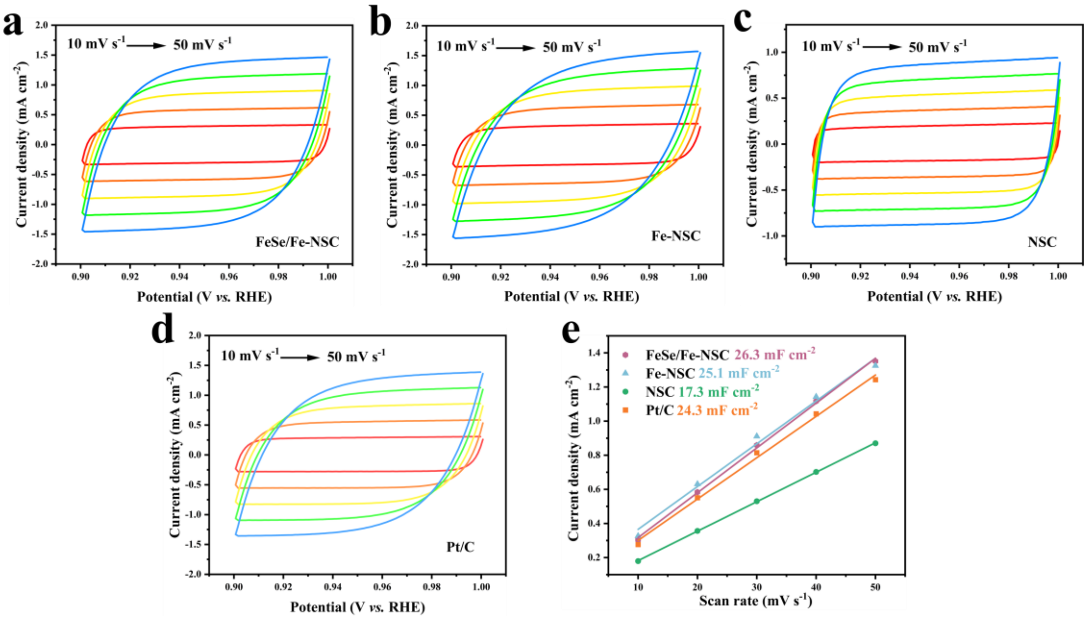

Fig. S21 CV curves of (a) FeSe/Fe-NSC, (b) Fe-NSC, (c) NSC, (d) Pt/C, and (e) Calculated C_{dl} values in 3.5 wt% NaCl.

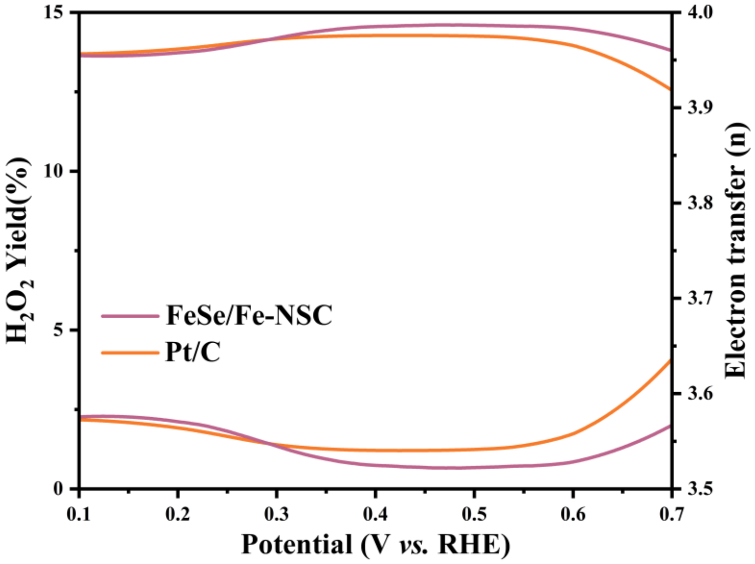

Fig. S22 Electron transfer number (n) and H_2O_2 yield of FeSe/Fe-NSC and Pt/C in 3.5 wt.% NaCl.

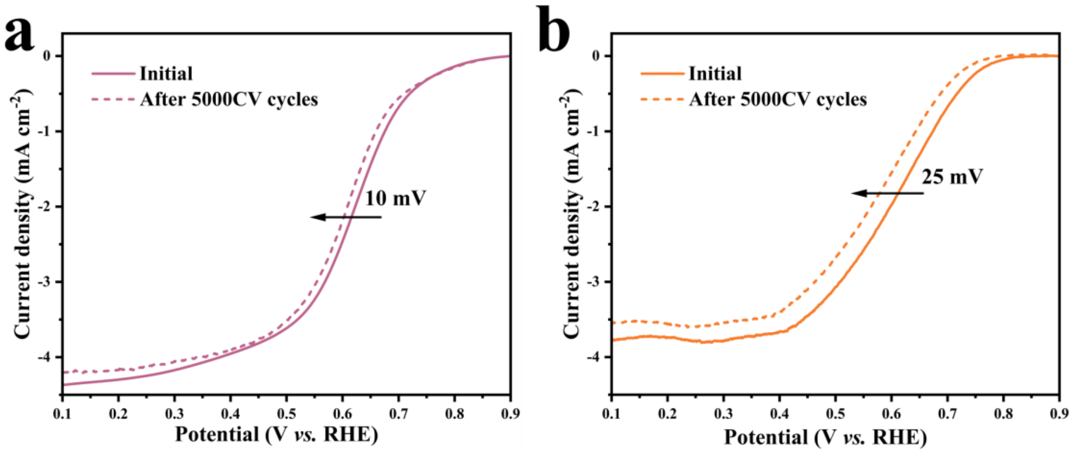

Fig. S23 LSV polarization curves of (a) FeSe/Fe-NSC and (b) commercial Pt/C before and after 5000 CV cycles in 3.5 wt% NaCl.

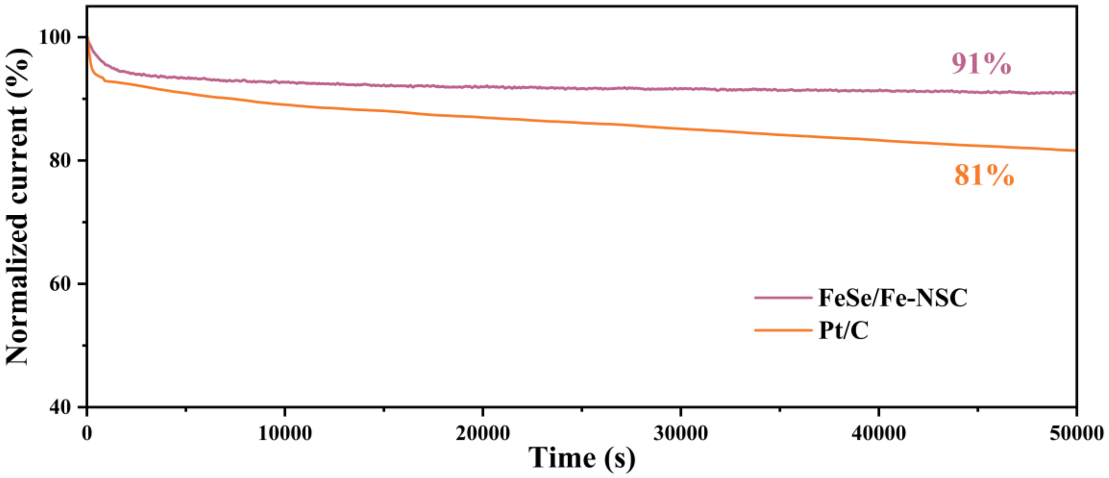

Fig. S24 Normalized chronoamperometric curves of FeSe/Fe-NSC and Pt/C in 3.5 wt% NaCl.

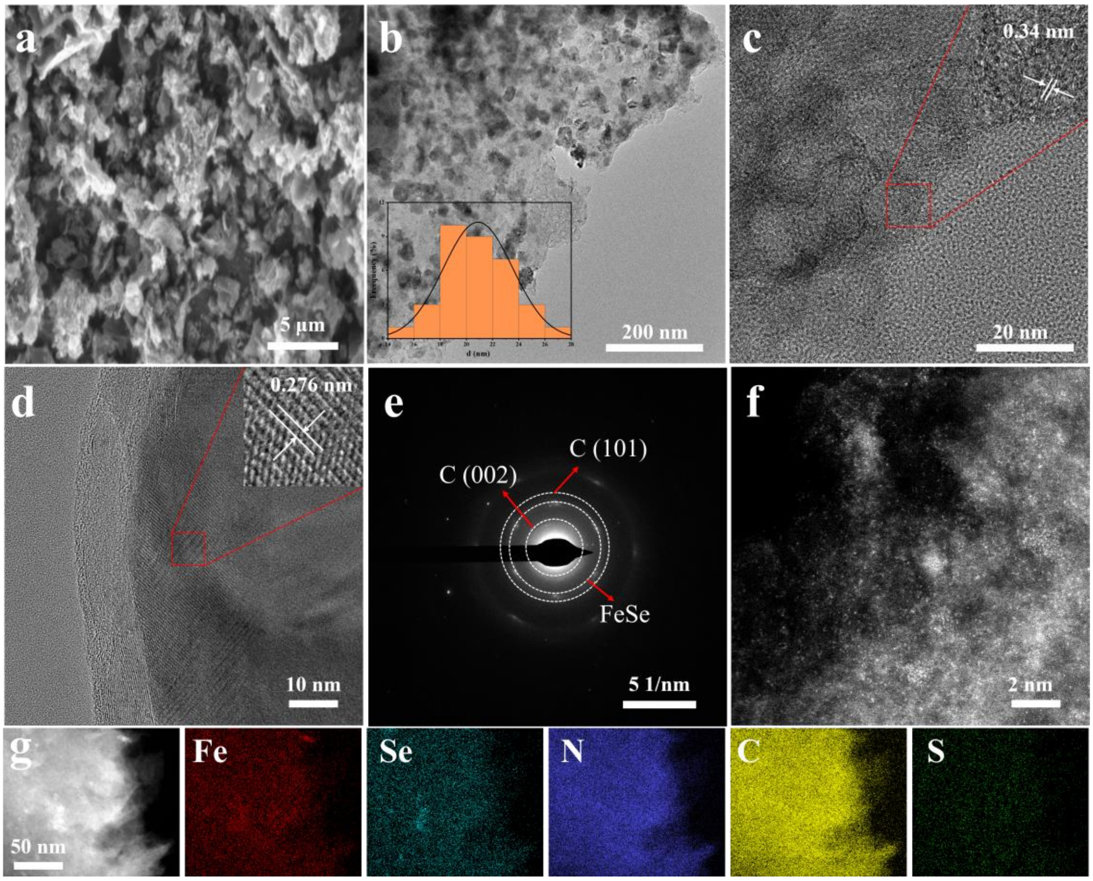

Fig. S25 Physical characterization of FeSe/Fe-NSC after 5000 CV cycles in 0.1 M KOH. (a) SEM image. (b) TEM image. (c) HR-TEM image and magnified view revealing carbon stripes. (d) HR-TEM image and magnified view resolving lattice fringes of FeSe NPs. (e) SAED pattern. (f) AC HAADF-STEM image highlighting single atoms and FeSe NPs. (g) EDS elemental mappings.

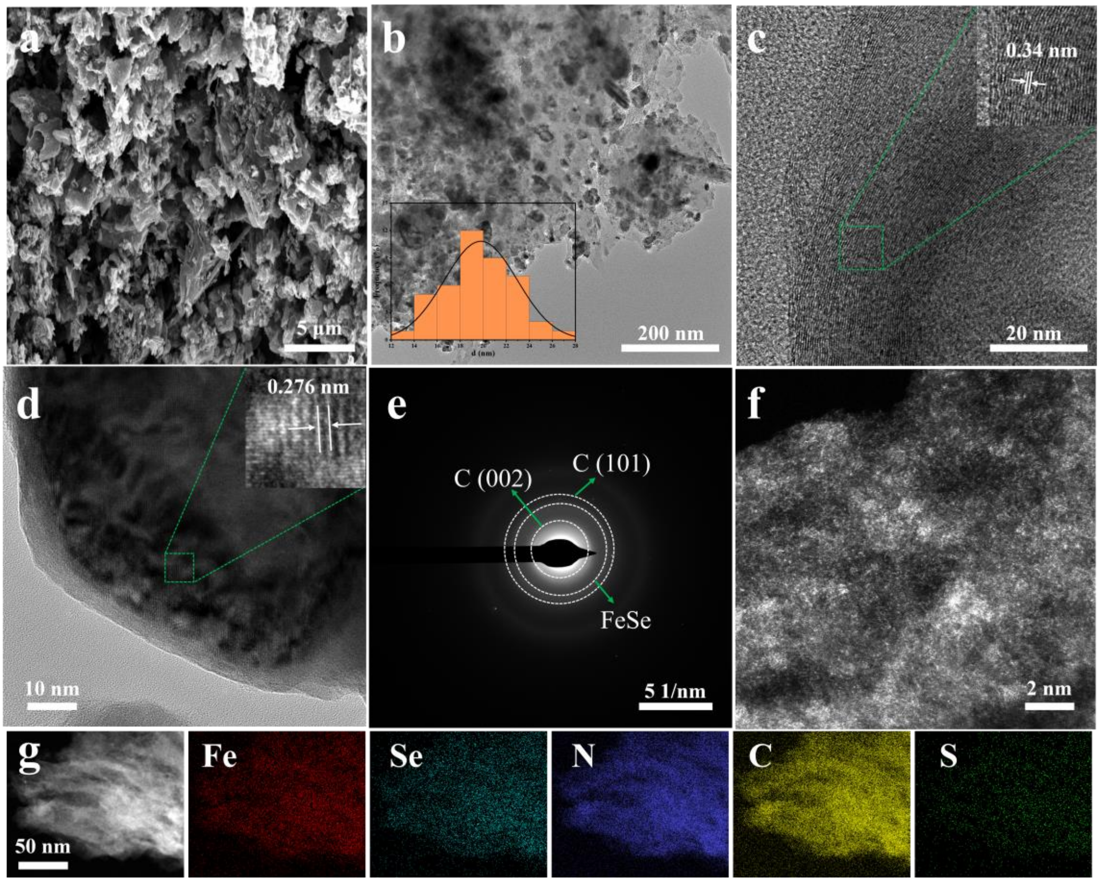

Fig. S26 Physical characterization of FeSe/Fe-NSC after 5000 CV cycles in 3.5 wt.% NaCl. (a) SEM image. (b) TEM image. (c) HR-TEM image and magnified view revealing carbon stripes. (d) HR-TEM image and magnified view resolving lattice fringes of FeSe NPs. (e) SAED pattern. (f) AC HAADF-STEM image highlighting single atoms and FeSe NPs. (g) EDS elemental mappings.

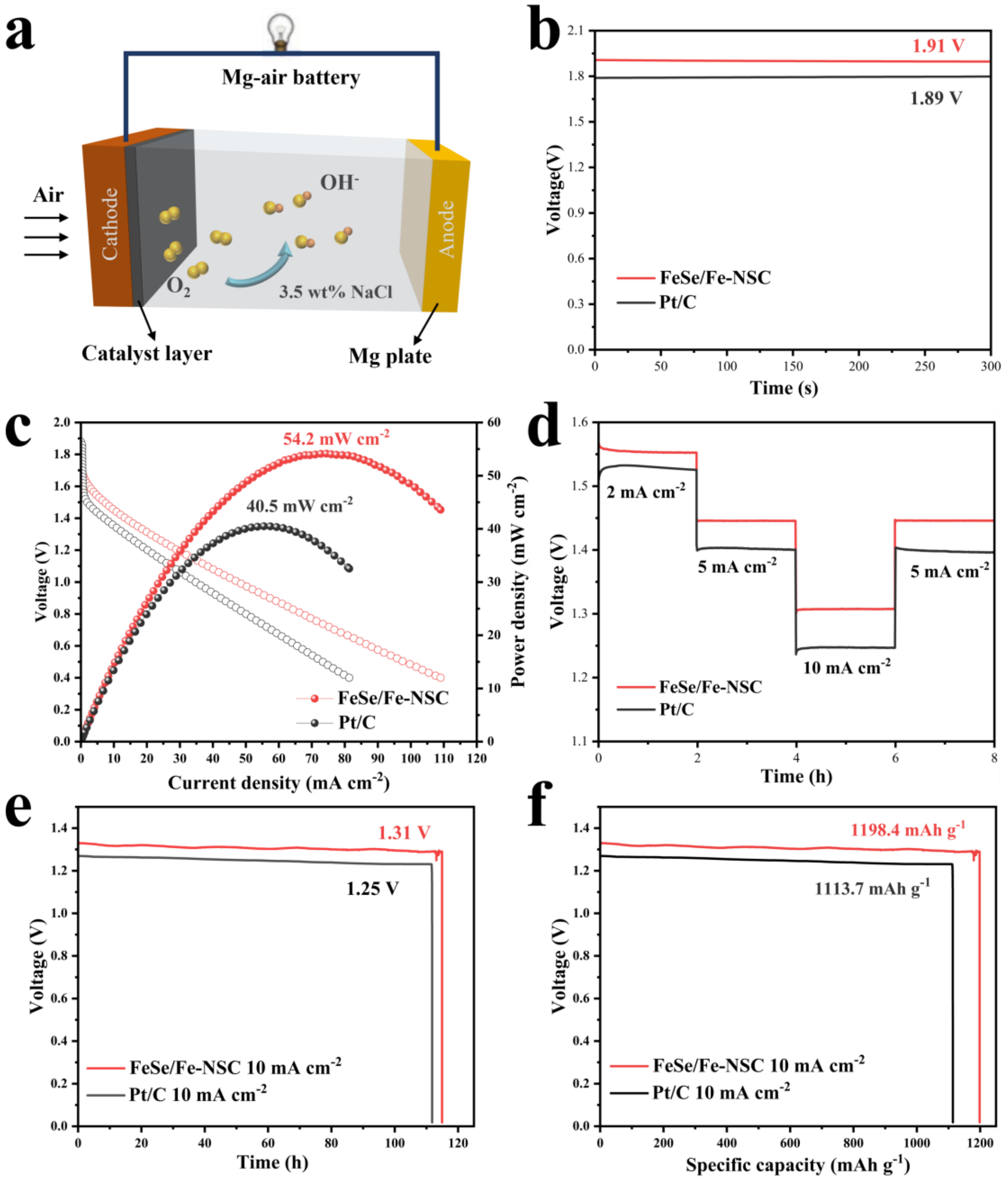

Fig. S27 Performance of assembled Mg-air battery. (a) Schematics of battery configuration. (b) Open-circuit voltages. (c) Discharge polarization and power densities. (d) Discharge voltage profiles at different current densities. (e) Galvanostatic discharge curves and (f) Specific capacities. The etectrolyte is 3.5 wt% NaCl.

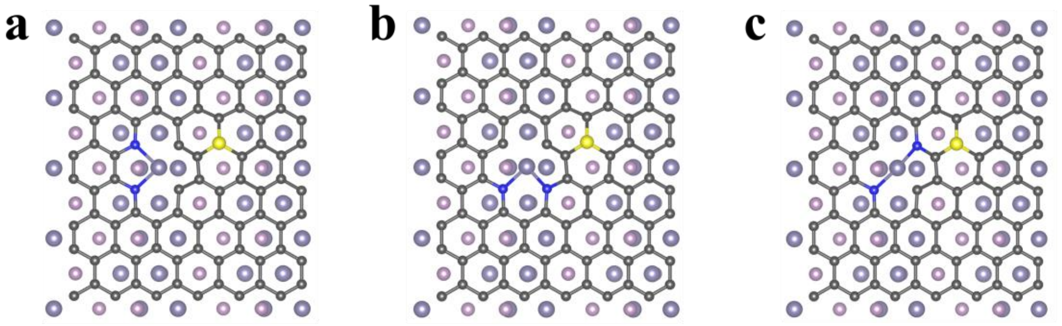

FeSe/Fe-NSC Formation energy: -2.17 eV

FeSe/Fe-NSC-1 Formation energy: -2.09 eV

FeSe/Fe-NSC-2 Formation energy: -2.07 eV

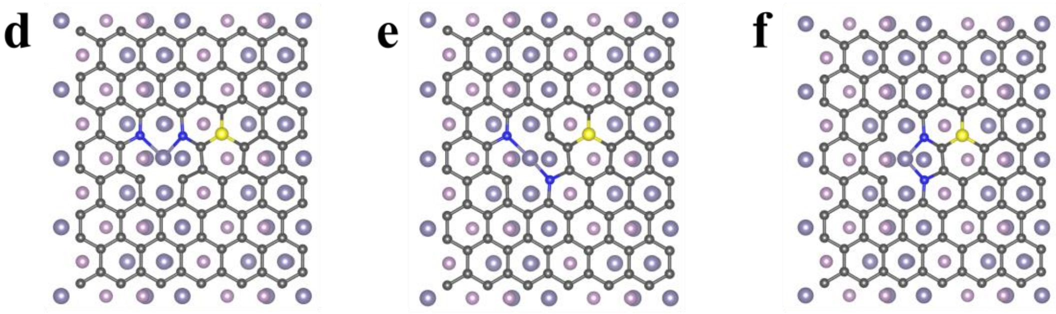

FeSe/Fe-NSC-3 Formation energy: -1.87 eV

FeSe/Fe-NSC-4 Formation energy: -1.83 eV

FeSe/Fe-NSC-5 Formation energy: -1.92 eV

Fig. S28 (a-f) Optimized geometric models and corresponding formation energy of FeSe/Fe-NSC with Fe−N_2 sites and FeSe NPs.

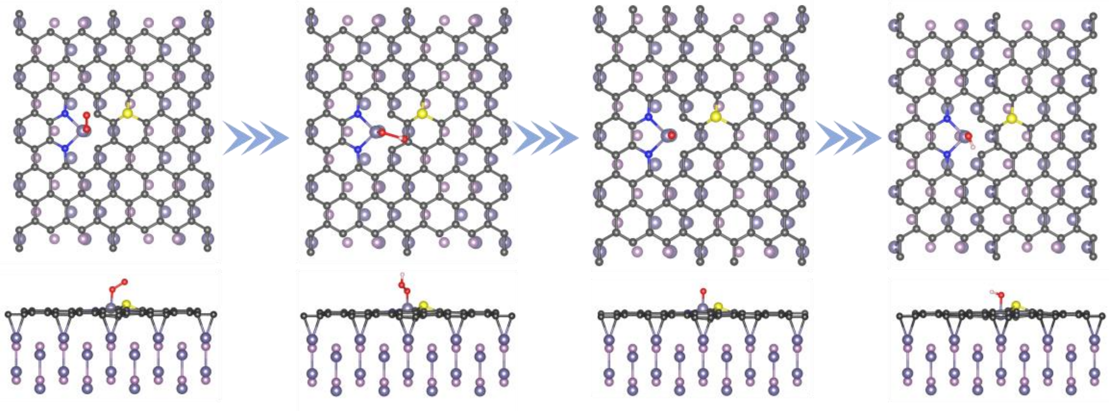

Fig. S29 Top and side views of optimized configurations for oxygen-containing intermediates (O_2, OOH*, O*, and OH*) adsorbed on FeSe/Fe-NSC(Fe−N_2).

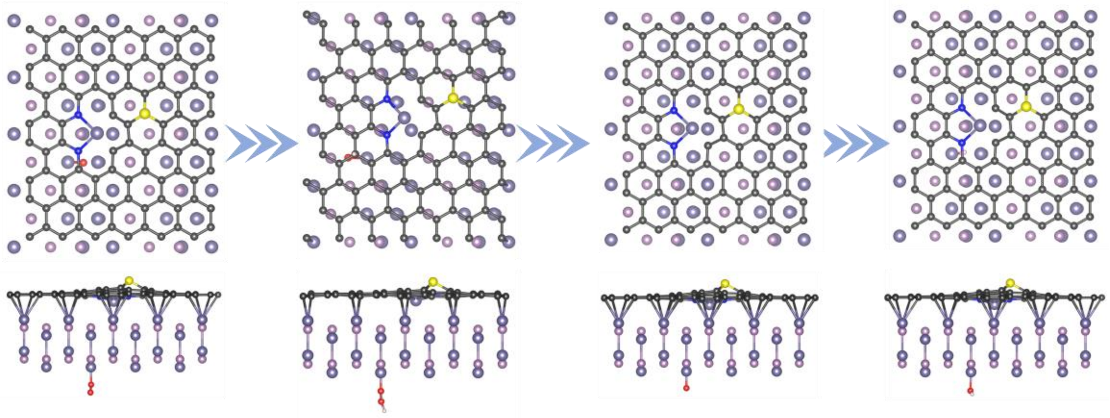

Fig. S30 Top and side views of optimized configurations for oxygen-containing intermediates (O_2, OOH*, O*, and OH*) adsorbed on FeSe/Fe-NSC(FeSe).

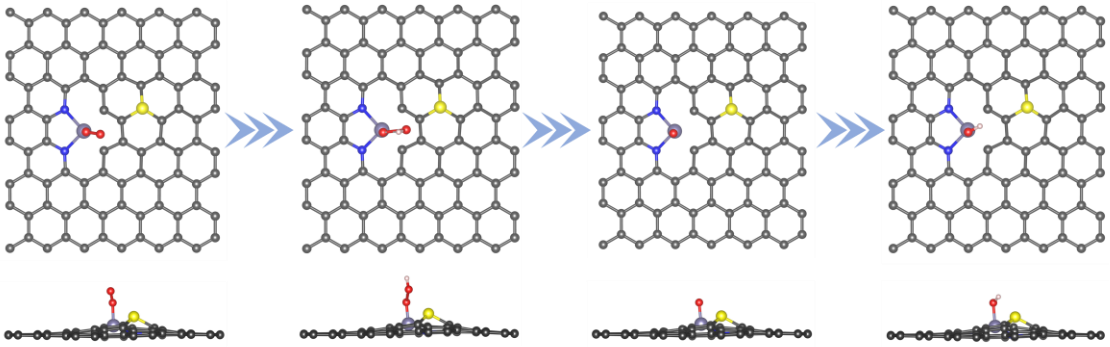

Fig. S31 Top and side views of optimized configurations for oxygen-containing intermediates (O_2, OOH*, O*, and OH*) adsorbed on Fe-NSC.

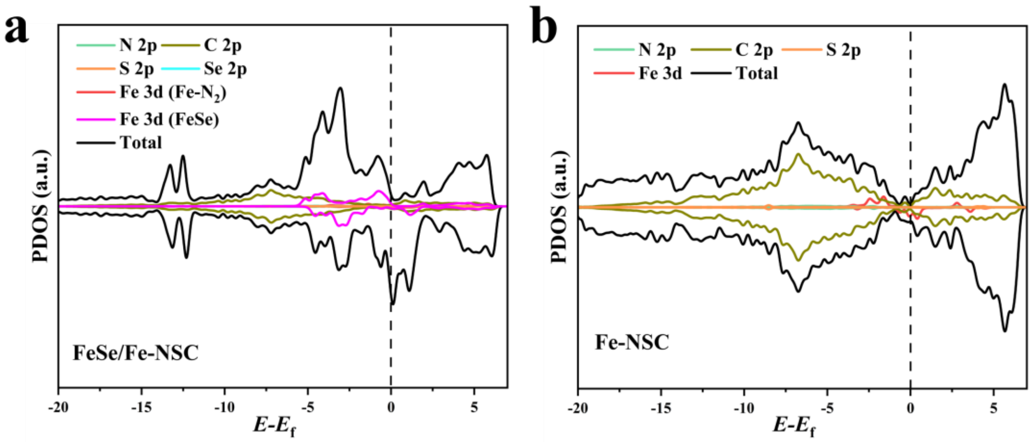

Fig. S32 PDOS of (a) FeSe/Fe-NSC and (b) FeSe/Fe-NSC.

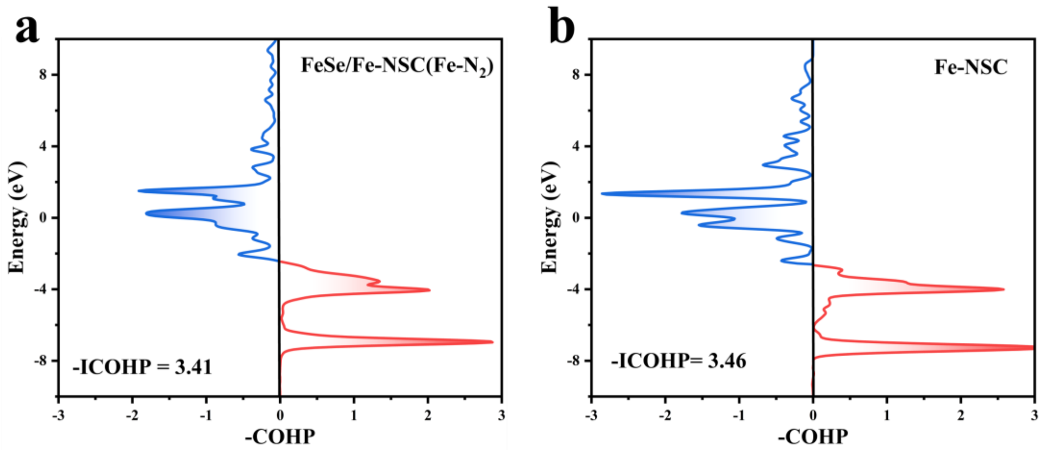

Fig. S33 ICOHP analysis of OH* adsorbed on (a) FeSe/Fe-NSC(Fe−N$_2$) and (b) Fe-NSC systems.

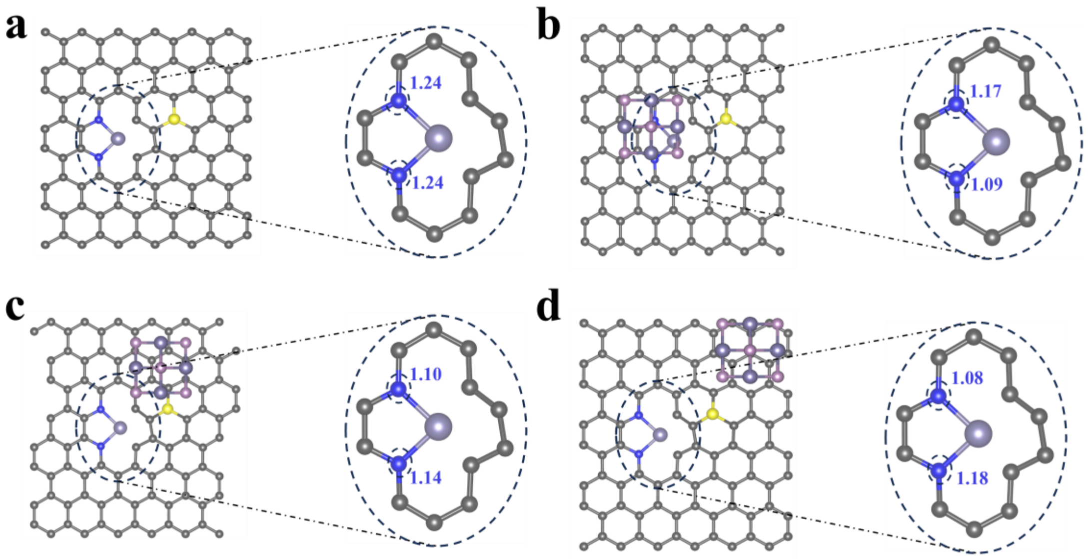

Fig. S34 Bader charges of N atoms in the local coordination around Fe sites in (a) Fe-NSC, (b) FeSe/Fe-NSC-S, (c) FeSe/Fe-NSC-M, and (d) FeSe/Fe-NSC-L.

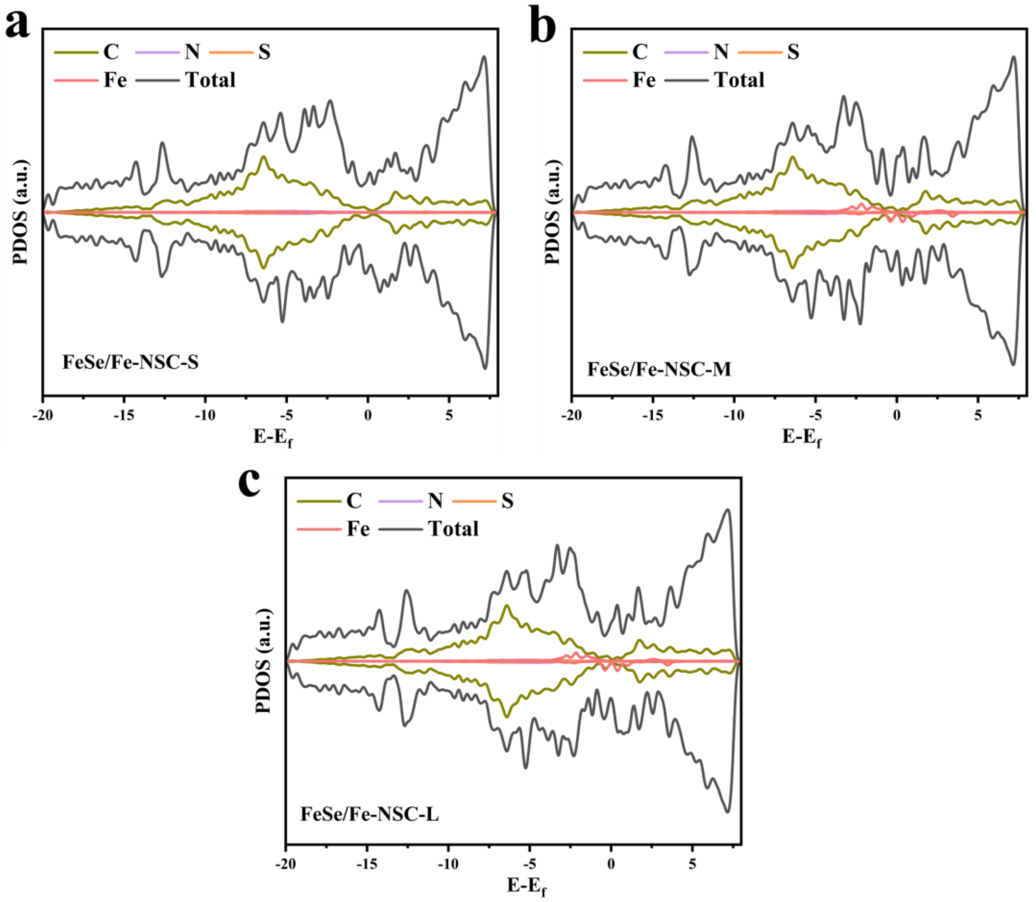

Fig. S35 PDOS for (a) FeSe/Fe-NSC-S, (b) FeSe/Fe-NSC-M, and (c) FeSe/Fe-NSC-L.

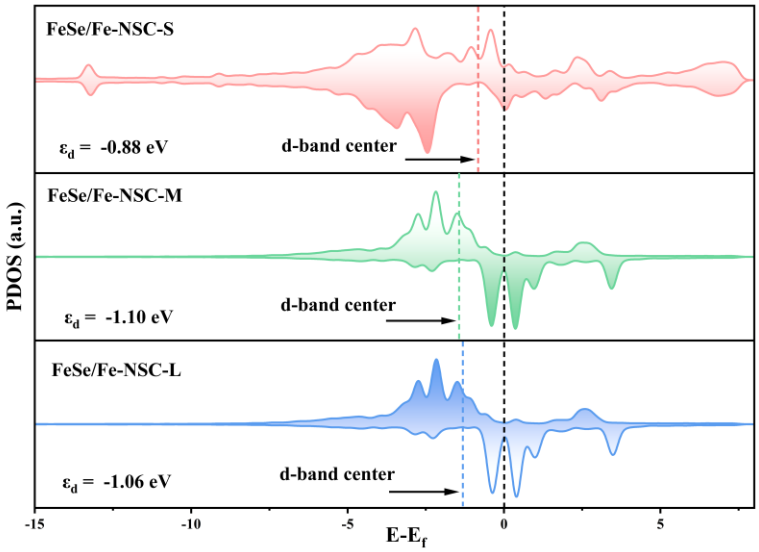

Fig. S36 The PDOS of the d-orbitals with d-band centers at the Fe active sites across the three models.

Table S1. Specific surface area, average pore size, and total pore volume.

Catalysts	Specific surface area (m^2 g^{-1})	Average pore size (nm)	Total pore volume (cm^3 g^{-1})
FeSe/Fe-NSC	512.6	7.11	0.83
Fe-NSC	485.3	6.32	0.76
NSC	468.8	4.91	0.63

Table S2. Relative percentages of N species based on the analysis of N 1s spectra.

Catalysts	Pyridinic-N (%)	M-N (%)	Pyrrolic-N (%)	Graphitic-N (%)
FeSe/Fe-NSC	36.96	19.97	15.11	27.96
Fe-NSC	37.78	16.02	22.98	23.22
NSC	48.04	-	24.24	27.72

Table S3. Structural parameters extracted from the Fe K-edge EXAFS fitting. (S_0^2=0.74)

Condition	**Pair**	***CN***	***R*(Å)**	**$\sigma^2(10^{-3}Å^2)$**	**ΔE_0(eV)**	**R factor**
Fe foil	Fe-Fe	8*	2.47±0.01	5.0±1.1	6.1±1.9	0.003
	Fe-Fe	6*	2.84±0.02	6.2±2.2	4.5±3.4	
FeSe/Fe-NSC	Fe-N	1.7±0.3	1.97±0.02	6.3±0.6	2.2±0.4	0.02
	Fe-Se	3.8±0.3	2.41±0.01	7.0±0.7	0.3±3.2	

S_0^2 is the amplitude reduction factor; CN is the coordination number; R is the interatomic distance (the bond length between the central atoms and surrounding coordination atoms); σ^2 is Debye-Waller factor (a measure of thermal and static disorder in absorber-scatterer distances); ΔE_0 is edge energy shift (the difference between the zero kinetic energy value of the sample and that of the theoretical model); R factor is used to evaluate the goodness of fitting.

Table S4. Metal contents of FeSe/Fe-NSC measured using ICP-AES.

Catalysts	**Fe (wt%)**	**Se (wt%)**
FeSe/Fe-NSC	5.75	4.05

Table S5. Comparison of ORR catalytic performance between FeSe/Fe-NSC and other previously reported non-precious metal catalysts in 0.1 M KOH.

Catalysts	***E*onset (V *vs*. RHE)**	**$E_{1/2}$ (V *vs*. RHE)**	**Ref.**
FeSe/Fe-NSC	**1.01**	**0.91**	**This work**
Fe-NSC	0.95	0.85	This work
NSC	0.91	0.81	This work
Pt/C	0.94	0.85	This work
Fe-NC-S	0.96	0.88	5
Fe SA-NSC-900	0.94	0.86	6
Fe_1Se_1-NC	1.00	0.88	7
Fe-Co-NC	0.98	0.88	8
Fe/Co-N-C	1.04	0.92	9
Fe/N/S-PCNT	0.96	0.84	10
Zn/Fe-N-C	1.08	0.86	11
FeNC-S-Fe_xC/Fe	1.05	0.87	12
Fe_1-HNC-500-850	0.91	0.83	13
Fe SA/NCZ	1.06	0.87	14
Fe/SNCFs-NH_3	1.02	0.89	15
Fe SAs-Fe_2P NPs/NPCFs-2.5	1.03	0.91	16
HPFe-N-C	-	0.91	17
FeS/Fe_3C@Fe-N-C	0.99	0.91	18
CoFe@C	0.98	0.89	19

Table S6. Comparison of ORR catalytic performance between FeSe/Fe-NSC and other previously reported non-precious metal catalysts in neutral brine electrolyte.

Catalysts	**Electrolyte**	**$E_{1/2}$ (V *vs.* RHE)**	**Ref.**
FeSe/Fe-NSC	**3.5 wt% NaCl**	**0.61**	**This work**
Fe-NSC	3.5 wt% NaCl	0.58	This work
NSC	3.5 wt% NaCl	0.51	This work
Pt/C	3.5 wt% NaCl	0.61	This work
Fe-Nx/NAC	3.5 wt% NaCl	0.59	20
CoNi-NCF	3.5 wt% NaCl	0.64	21
CoZn/NC	3.5 wt% NaCl	0.58	22
CoFe@CoFe-N-C	3.5 wt% NaCl	0.61	23
2D N-S-CNS	3.5 wt% NaCl	0.60	24
CuCo@N/C-800	3.5 wt% NaCl	0.52	25
CoFe@NC-600	3.5 wt% NaCl	0.52	26
Fe/Cu-N-C	3.5 wt% NaCl	0.60	27
CCO-600	3.5 wt% NaCl	0.38	28
Fe/N/C	0.5 M NaCl	0.57	29
$SMO_{4.86}$	1 M NaCl	0.48	30
Mn-NC	1 M NaCl	0.51	31
Co/NNC	1 M NaCl	0.60	32
$Co_{0.2}$Mn-NC	1 M NaCl	0.59	33
Co/CoO/Co_3O_4/NSC	1 M NaCl	0.55	34
Co@FLG-40	1 M NaCl	0.51	35

Table S7. Performance comparison of Zn-air batteries adopting FeSe/Fe-NSC and other previously reported non-precious metal catalysts.

Catalysts	**Peak power density ($mW\ cm^{-2}$)**	**Specific Capacity ($mAh\ g^{-1}$)**	**Ref.**
FeSe/Fe-NSC	**116.6**	**815.4**	**This work**
Fe-N_x-C	96.4	641	36
CoNi-SAs/NC	101.4	750.9	37
C-FeZIF-8@g-C_3N_4	121.0	694	38
Fe-N-C/N-OMC	113	711	39
CoN_4/NG	115	730	40
F-FeNC	141	760	41
Fe-N-C-800	135.3	744	42
FeP/Fe_2O_3@NPCA	130	717	43
FeS/Fe_3C@NS-C-900	90.9	750	44
Co_4N@NC-2	74.3	769.4	45
Fe,Mn/N-C	160.8	902	46
Co SA/NCFs	154.5	796	47
Fe-OAC	113	710	48
Fe-N-C/rGO	107.1	736.7	49
P-FeCo/NC	115	760.4	50
CoNP@FeNC-0.05	104.4	-	51

Table S8. Performance comparison of Mg-air batteries adopting FeSe/Fe-NSC and other previously reported non-precious metal catalysts.

Catalysts	**Electrolyte**	**Peak power density ($mW\ cm^{-2}$)**	**Ref.**
FeSe/Fe-NSC	**3.5 wt% NaCl**	**54.2**	**This work**
CuCo@NC-800	3.5 wt% NaCl	17.3	25
CoZn/NC	3.5 wt% NaCl	28.0	22
CoFe@NC-600	3.5 wt% NaCl	17.5	26
CoFe@Co/Fe-N-C	3.5 wt% NaCl	24.8	23
CCO-600	3.5 wt% NaCl	13.6	28
Fe/Cu-N-C	3.5 wt% NaCl	49.7	27
Co-NCNT	10 wt% NaCl	58.6	52
N-MnO_2	10 wt% NaCl	124.3	53
Ag@α-MnO_2	10 wt% NaCl	107.2	54
Fe,Ni-SAs/DNSC	10 wt% KCl	76.0	55
MC-140-12-10	15 wt% NaCl	74.0	56
Co/NNC	1M NaCl	118.3	32
$NiCoN_x$/CNT	1M NaCl	112.4	57
Co/CoO/Co_3O_4/NSC	1M NaCl	111.8	34
$SMO_{4.86}$	1M NaCl	101.0	30
Co@FLG-40	1M NaCl	66.0	35
US ON	5M NaCl	73.4	58

References

1 G. Kresse and J. Hafner, *Phys. Rev. B*, 1993, **47**, 558–561.

2 J. P. Perdew, K. Burke and M. Ernzerhof, *Phys. Rev. Lett.*, 1996, **77**, 3865–3868.

3 P. E. Blöchl, *Phys. Rev. B*, 1994, **50**, 17953–17979.

4 G. Kresse and D. Joubert, *Phys. Rev. B*, 1999, **59**, 1758–1775.

5 X. Li, C.-S. Cao, S.-F. Hung, Y.-R. Lu, W. Cai, A. I. Rykov, S. Miao, S. Xi, H. Yang, Z. Hu, J. Wang, J. Zhao, E. E. Alp, W. Xu, T.-S. Chan, H. Chen, Q. Xiong, H. Xiao, Y. Huang, J. Li, T. Zhang and B. Liu, *Chem*, 2020, **6**, 3440–3454.

6 M. Wang, W. Yang, X. Li, Y. Xu, L. Zheng, C. Su and B. Liu, *ACS Energy Lett.*, 2021, **6**, 379–386.

7 Z. Chen, X. Su, J. Ding, N. Yang, W. Zuo, Q. He, Z. Wei, Q. Zhang, J. Huang and Y. Zhai, *Appl. Catal. B: Environ, Energy.*, 2022, **308**, 121206.

8 L. Wu, Y. Chen, C. Shao, L. Wang and B. Li, *Adv. Funct. Mater.*, 2024, **34**, 2408257.

9 R. Dun, X. He, J. Huang, W. Wang, Yiwei liu, L. Li, B. Lu, Z. Hua and J. Shi, *J. Mater. Chem. A*, 2023, **11**, 5902–5909.

10 Z. Tan, H. Li, Q. Feng, L. Jiang, H. Pan, Z. Huang, Q. Zhou, H. Zhou, S. Ma and Y. Kuang, *J. Mater. Chem. A*, 2019, **7**, 1607–1615.

11 J. Xue, Y. Li and J. Hu, *J. Mater. Chem. A*, 2020, **8**, 7145–7157.

12 Y. Qiao, P. Yuan, Y. Hu, J. Zhang, S. Mu, J. Zhou, H. Li, H. Xia, J. He and Q. Xu, *Adv. Mater.*, 2018, **30**, 1804504.

13 X. Zhang, S. Zhang, Y. Yang, L. Wang, Z. Mu, H. Zhu, X. Zhu, H. Xing, H. Xia, B. Huang, J. Li, S. Guo and E. Wang, *Adv. Mater.*, 2020, **32**, 1906905.

14 C. Jiao, Z. Xu, J. Shao, Y. Xia, J. Tseng, G. Ren, N. Zhang, P. Liu, C. Liu, G. Li, S. Chen, S. Chen and H.-L. Wang, *Adv. Funct. Mater.*, 2023, **33**, 2213897.

15 L. Yang, X. Zhang, L. Yu, J. Hou, Z. Zhou and R. Lv, *Advanced Materials*, 2022, **34**, 2105410.

16 Y. Pan, X. Ma, M. Wang, X. Yang, S. Liu, H.-C. Chen, Z. Zhuang, Y. Zhang, W.-C. Cheong, C. Zhang, X. Cao, R. Shen, Q. Xu, W. Zhu, Y. Liu, X. Wang, X. Zhang, W. Yan, J. Li, H. M. Chen, C. Chen and Y. Li, *Adv. Mater.*, 2022, **34**, 2203621.

17 H. Xu, D. Wang, P. Yang, L. Du, X. Lu, R. Li, L. Liu, J. Zhang and M. An, *Appl. Catal. B: Environ, Energy.*, 2022, **305**, 121040.

18 S. Sun, F. Yang, X. Zhang, J. Qian, K. Wei, J. An, Y. Sun, S. Wang, X. Li and Y. Li, *Chem. Eng. J.*, 2024, **487**, 150673.

19 D. Ren, J. Ying, M. Xiao, Y.-P. Deng, J. Ou, J. Zhu, G. Liu, Y. Pei, S. Li, A. M. Jauhar, H. Jin, S. Wang, D. Su, A. Yu and Z. Chen, *Adv. Funct. Mater.*, 2020, **30**, 1908167.

20 Y. Zhan, Z.-B. Ding, F. He, X. Lv, W.-F. Wu, B. Lei, Y. Liu and X. Yan, *Chem. Eng. J.*, 2022, **443**, 136456.

21 M. Jiang, J. Yang, J. Ju, W. Zhang, L. He, J. Zhang, C. Fu and B. Sun, *Energy Storage Mater.*, 2020, **27**, 96–108.

22 J. Chen, B. Feng, W. Wang, Y. Liang, W. Zhang, X. Li, C. Li, N. Wang and Z. Shi, *J. Alloys Compd.*, 2024, **983**, 173878.

23 N. Wang, J. Liang, J. Liu, Q. Cai, J. Li, J. Chen, T. Huang and Z. Shi, *J. Power Sources*, 2022, **517**, 230707.

24 R. Cheng, M. Jiang, K. Li, M. Guo, J. Zhang, J. Ren, P. Meng, R. Li and C. Fu, *Chem. Eng. J.*, 2021, **425**, 130603.

25 X. Dong, J. Wang, X. Wang, J. Xu, J. Yang, W. Zeng, Y. Li, Y. Zhao, G. Huang, J. Wang and F. Pan, *ChemElectroChem*, 2022, **9**, e202200585.

26 X. Dong, J. Wang, X. Wang, J. Xu, J. Yang, W. Zeng, Y. Zhang, G. Huang, J. Wang and F. Pan, *ACS Appl. Energy Mater.*, 2022, **5**, 12272–12282.

27 W. Zhang, B. Feng, L. Huang, Y. Liang, J. Chen, X. Li, Z. Shi and N. Wang, *Appl. Catal. B: Environ, Energy.*, 2024, **358**, 124450.

28 X. Dong, J. Wang, X. Wang, J. Yang, L. Zhu, W. Zeng, G. Huang, J. Wang and F. Pan, *J. Electrochem. Soc.*, 2022, **169**, 010532.

29 A. Asokan, S. Abu-Khalla, S. Abdalla and M. E. Suss, *ACS Appl. Energy Mater.*, 2022, **5**, 1743–1754.

30 X. Zhao, L. Wang, X. Chen, W. Wang, H. L. Xin, X. Du and J. Yang, *J. Power Sources*, 2020, **449**, 227482.

31 Q. Li, T. Zhao, C. He, Y. Cai, Q. Wu, Y. Huang, K. Liu, Z. Ma and H. Wang, *Electrochim. Acta*, 2022, **410**, 139975.

32 X. Wu, C. Tan, C. He, T. Zhao, X. Wu, Z. Ma, H. Wang, Y. Cai, Q. Wu and Q. Li, *J. Power Sources*, 2022, **520**, 230891.

33 T. Zhao, S. Niu, X. Wu, Q. Wu, Z. Ma, J. Jiang, Y. Huang, H. Wang, Q. Li and Y. Cai, *J. Alloys Compd.*, 2022, **924**, 166532.

34 X. Wu, Z. Zhang, C. He, Y. Shen, X. Wu, H. Wang, Z. Ma and Q. Li, *Chem. Eng. J.*, 2023, **453**, 139831.

35 K. Zhao, S. Liu, G. Ye, X. Wei, Y. Su, W. Zhu, Z. Zhou and Z. He, *ChemSusChem*, 2020, **13**, 1556–1567.

36 J. Han, X. Meng, L. Lu, J. Bian, Z. Li and C. Sun, *Adv. Funct. Mater.*, 2019, **29**, 1808872.

37 X. Han, X. Ling, D. Yu, D. Xie, L. Li, S. Peng, C. Zhong, N. Zhao, Y. Deng and W. Hu, *Adv. Mater.*, 2019, **31**, 1905622.

38 Y. Deng, X. Tian, B. Chi, Q. Wang, W. Ni, Y. Gao, Z. Liu, J. Luo, C. Lin, L. Ling, F. Cheng, Y. Zhang, S. Liao and S. Zhang, *Chem. Eng. J.*, 2020, **390**, 124479.

39 J. Han, H. Bao, J.-Q. Wang, L. Zheng, S. Sun, Z. L. Wang and C. Sun, *Appl. Catal. B: Environ, Energy.*, 2021, **280**, 119411.

40 L. Yang, L. Shi, D. Wang, Y. Lv and D. Cao, *Nano Energy*, 2018, **50**, 691–698.

41 T. Yang, Y. Chen, M. Tian, X. Liu, F. Zhang, J. Zhang, K. Wang and S. Gao, *Electrochim. Acta*, 2023, **443**, 141907.

42 D. Wang, L. Xiao, P. Yang, Z. Xu, X. Lu, L. Du, O. Levin, L. Ge, X. Pan, J. Zhang and M. An, *J. Mater. Chem. A*, 2019, **7**, 11007–11015.

43 K. Wu, L. Zhang, Y. Yuan, L. Zhong, Z. Chen, X. Chi, H. Lu, Z. Chen, R. Zou, T. Li, C. Jiang, Y. Chen, X. Peng and J. Lu, *Adv. Mater.*, 2020, **32**, 2002292.

44 Y.-W. Li, W.-J. Zhang, J. Li, H.-Y. Ma, H.-M. Du, D.-C. Li, S.-N. Wang, J.-S. Zhao, J.-M. Dou and L. Xu, *ACS Appl. Mater. Interfaces*, 2020, **12**, 44710–44719.

45 H. Ge, G. Li, J. Shen, W. Ma, X. Meng and L. Xu, *Appl. Catal. B: Environ, Energy.*, 2020, **275**, 119104.

46 G. Yang, J. Zhu, P. Yuan, Y. Hu, G. Qu, B.-A. Lu, X. Xue, H. Yin, W. Cheng, J.

Cheng, W. Xu, J. Li, J. Hu, S. Mu and J.-N. Zhang, *Nat. Commun*, 2021, **12**, 1734.

47 Y. Han, H. Duan, C. Zhou, H. Meng, Q. Jiang, B. Wang, W. Yan and R. Zhang, *Nano Lett.*, 2022, **22**, 2497–2505.

48 L. Deng, L. Qiu, R. Hu, L. Yao, Z. Zheng, X. Ren, Y. Li and C. He, *Appl. Catal. B: Environ, Energy.*, 2022, **305**, 121058.

49 L. Li, Y.-J. Chen, H.-R. Xing, N. Li, J.-W. Xia, X.-Y. Qian, H. Xu, W.-Z. Li, F.-X. Yin, G.-Y. He and H.-Q. Chen, *Nano Res.*, 2022, **15**, 8056–8064.

50 N. Wang, R. Mei, L. Chen, T. Yang, Z. Chen, X. Lin and Q. Liu, *Small*, 2024, **20**, 2400327.

51 Y. Xue, Y. Guo, Q. Zhang, Z. Xie, J. Wei and Z. Zhou, *Nano-Micro Lett.*, 2022, **14**, 162.

52 Q. Liao, G. Li, R. Ding, Z. He, M. Jiang, C. Zhao, T. Li, X. Liu, S. Chen and H. He, *Int. J. Hydrogen Energy*, 2021, **46**, 31253–31261.

53 X. Liu, Z. He, T. Li, X. Wang, C. Zhao, S. Liu, Y. Liu, Z. Fan and H. He, *J. Mater. Sci.*, 2023, **58**, 3066–3077.

54 G. Li, M. Jiang, Q. Liao, R. Ding, Y. Gao, L. Jiang, D. Zhang, S. Chen and H. He, *J. Alloys Compd.*, 2021, **858**, 157672.

55 X. Zhang, Y. Li, M. Jiang, J. Wei, X. Ding, C. Zhu, H. He, H. Lai and J. Shi, *Chem. Eng. J.*, 2021, **426**, 130758.

56 H. Liu, J. Song, J. Zhang, Z. Li, H. Fang, Q. Zhang, X. He, C. Lu, W. Xu and K. Yu, *J. Electrochem. Soc.*, 2022, **169**, 090508.

57 X. Chen, X. Yu, G. Zhang, S. Wei, Y. Huang, H. Wang, J. Jiang, Z. Ma and Q. Li,

J. Electroanal. Chem., 2024, **958**, 118162.

58 H. Huang, P. Liu, Q. Ma, Z. Tang, M. Wang and J. Hu, *Energy*, 2023, **270**, 126991.